Assymetry and Thermal Effects Due to Parellel Motion of Electrons in Collisionless Magnetic Reconnection

Motohiko Tanaka

RLE Technical Report No. 609

January 1997

This work has been sponsored in part by the US Department of Energy.

The Research Laboratory of Electronics
MASSACHUSETTS INSTITUTE OF TECHNOLOGY
CAMBRIDGE, MASSACHUSETTS 02139-4307

Abstract

Fast collisionless reconnection of magnetic flux loops by the macro-particle simulation study shows significant asymmetry of the plasma flow under an ambient toroidal magnetic field. The parallel motion of electrons induced by the reconnection electric field is found to produce large density and toroidal magnetic field inhomogeneities of a quadrupole shape, $\delta n/n_0 \sim 0.3$, unlike the m=1 mode. The divergence of the plasma flow is locally not identical to zero with each species, $\nabla \cdot \mathbf{V}^{(s)} \neq 0$ $(s = e, i)$, due to the electron spatial movement along the magnetic field. This internal structure results in a thick current layer to enhance the reconnection process. A plasmoid that impedes magnetic reconnection is created when the parallel mass diffusivity of electrons arising from their thermal motion is suppressed (the fluid limit). The reconnection rate becomes a smoothly increasing function of the ion mass and an inverse of the toroidal magnetic field, the latter of which being due to the compressional effect. The rate is drastically reduced when the ion Larmor radius far exceeds the ion skin depth.

PACS Numbers: 52.30., 52.35P, 52.65, 95.30

1. Introduction

The formation of the current layer and its internal structure are important physics issues of fast magnetic reconnection, as they determine the nature of magnetic reconnection observed in solar flares, magnetosphere and fusion plasmas[1,2]. In order to investigate the fundamental processes of magnetic reconnection which is expected to occur in a collisionless state, non-resistive MHD (magnetohydrodynamic) studies were extensively performed by means of the fluid[3–6] and particle simulation methods[7–10]. These studies are classified into those of the m=1 mode[3–5] and the coalescence process[6–10] depending on whether adopted geometry of the plasma (magnetic field) is open or closed. The present paper will deal with the coalescence process which takes place in astrophysical and laboratory environments.

For the aforementioned purposes, a fully-kinetic study by the particle simulation codes[7–10] might be a highly desirable way to obtain the complete picture of collisionless reconnection from the first principle, as will be described in this paper. It is shown that both the fluid (bulk) and kinetic (thermal) effects of the electrons are essentially important in the study of collisionless reconnection process.

The previous study of collisionless reconnection of magnetic flux loops in the framework of the (incompressible) two-fluid theory showed a development of the infinitely thin (singular) current layer at the interface between the flux loops[6]. The symmetric initial conditions always resulted in completely symmetric plasma flows during the coalescence process. However, the symmetric solution was precisely due to the incompressibility assumption imposed on each plasma species. As a consequence, the plasma density stayed homogeneous and no internal structure could appear in the current layer. The thin channel of the current layer was the only path to escape for the plasma coming into the reconnection layer. The reconnection rate showed a steep increase at the small ion mass regime and weak dependence elsewhere, owing to the singular layer thickness at the small ion mass regime.

By contrast, it was found by the macro-particle simulation study[8] that during the reconnection of the flux loops, a thick current layer comparable to the electron skin depth[11] is formed which is associated with significantly asymmetric plasma flow. The asymmetry is proved here to be directly connected with divergence of the electron bulk flow along the

magnetic field. This new feature has an important consequence to magnetic reconnection: The substantially thick current layer is maintained through an appearance of the internal structure, i.e. asymmetric density and toroidal magnetic field variations, within the current layer arising from the electron parallel motion[10]. Since the reconnection rate scales as, $d\Psi/dt \sim v_A D/L$ with Ψ the isolated poloidal magnetic flux, D and L the thickness and length of the current layer, respectively, the asymmetry should increase the reconnection rate compared to the incompressible fluid case which is accompanied by the very thin current layer[6]. Also, the rate becomes a smoothly increasing function of the ion mass without a sudden curvature change because the thickness D is not singular at the small ion mass regime.

The electron thermal motion, generally speaking, is expected to accelerate the reconnection process. Such an effect may be approximated in terms of the enhanced diffusion of plasma pressure in the fluid study[5]. If electron mass diffusivity due to the thermal motion is not taken into account as in the ordinary fluid studies[4,6], a thin current layer and slower reconnection result. In the present study by the particle simulation code, a plasma with low electron temperature is found to create a plasmoid that holds the reconnection-blocking toroidal current and impedes the reconnection process (Sec.3.2). Again, divergence of the plasma flow, $\nabla \cdot \mathbf{V} \neq 0$, is required for development of the large *detached* plasmoid at the X-point. Reconnection takes place only after the plasmoid is pushed out of the current layer by plasma pressure. Therefore, it is essential in the study of collisionless magnetic reconnection to incorporate the mass diffusivity of the current-carrying electrons through their thermal motion along the magnetic field.

To avoid general confusion with the m=1 mode[3-5], it is stressed here that the coalescence of the flux loops is a fast reconnection process which occurs essentially in the system with open magnetic field geometry such as for the solar flares[12]. The process is strongly driven by the attractive force between the current of the same polarity which are contained in the flux loops. Accumulation of plasma pressure at the X-point is not enough to stabilize the merging process. On the other hand, the m=1 mode is a reconnection process slower than the coalescence process. It is because the tokamak plasma in which the m=1 mode grows is an equilibrium, magnetically-closed system. The plasma flow is confined in a narrow

channel between the nested flux surfaces.

In this paper, the asymmetric solution arising from compressibility of the plasma bulk flow is shown to be a natural solution of the collisionless coalescence process of the flux loops under the ambient magnetic field. Moreover, it is shown that the thermal motion of the electrons is required to avoid the plasmoid formation and to enhance the collisionless reconnection process. The role of finite ion Larmor radius is also presented.

An outline of this paper will be the following. In Sec.2, the numerical method and conditions adopted in the macro-particle simulations are presented. The simulation results are described in subsequent two sections: the roles of the asymmetric (bulk) flow and the thermal motion in Sec.3. Also in this section, the incompressible fluid limit is argued. In Sec.4, the parametric dependences of the reconnection rate on the ion mass, Larmor radius and the toroidal magnetic field are shown. Summary and conclusion will be made in Sec.5.

2. Simulation Method and Initial Conditions

Before the details of the simulations are shown, the macro-particle simulation code adopted in this study is briefly summarized to clarify its advantages over the standard electromagnetic and hybrid-particle codes.

The macro-particle code is the low-frequency, large spatial-scale simulation technique[9,13], using the time step Δt and spatial scale Δx such that $\omega_{pe}\Delta t \gg 1$ and $\Delta x/\lambda_{De} \gg 1$, where ω_{pe} and λ_{De} are, respectively, the plasma frequency and the Debye length. Note that the typical values used in the conventional electromagnetic particle code are $\omega_{pe}\Delta t \sim 0.2$ and $\Delta x/\lambda_{De} = 1$. The macro-particle code has both the full-kinetic and electron drift-kinetic versions in multi-dimensional coordinate space. In the codes, the Maxwell equations are solved for the electromagnetic field, except that the backward time-decentering scheme is introduced to realize the "mesoscale" characteristics just mentioned,

$$(\partial \mathbf{E}/\partial t)^{n+1/2} = c\nabla \times \mathbf{B}^{n+\alpha} - 4\pi \mathbf{J}^{n+\alpha}, \tag{1}$$

$$(\partial \mathbf{B}/\partial t)^{n+1/2} = -c\nabla \times \mathbf{E}^{n+\alpha}, \tag{2}$$

$$\nabla \cdot \mathbf{E}^{n+1} = 4\pi \rho^{n+1}, \tag{3}$$

$$\nabla \cdot \mathbf{B}^{n+1} = 0. \tag{4}$$

Here, $\mathbf{E}$ and $\mathbf{B}$ are the electric and magnetic fields, respectively, $\mathbf{J}$ and ρ the current and charge densities. The superscripts stand for the time level in the unit Δt on which each quantity is defined. The constant α ($> \frac{1}{2}$) gives time-implicitness which serves to filter out high-frequency components of the electromagnetic oscillations with $\omega\Delta t \geq O(1)$, where ω is their characteristic frequency. Therefore, large noises due to the high-frequency electromagnetic waves and the Langmuir oscillations which the standard electromagnetic particle code includes are eliminated in the present low-frequency particle simulation code.

The equations of motion for each particle are the Newton-Lorentz equations, again with the time-decentering technique,

$$(d\mathbf{x}_j/dt)^{n+1/2} = \mathbf{v}_j^{n+1/2}, \tag{5}$$

$$(d\mathbf{v}_j/dt)^{n+1/2} = (e_j/m_j)[\mathbf{E}^{n+\alpha} + (\mathbf{v}_j/c)^{n+1/2} \times \mathbf{B}^{n+\alpha}]. \tag{6}$$

When the electrons are well magnetized, the drift-kinetic equations are used,

$$(d\mathbf{x}_j/dt)^{n+1/2} = [v_{\|j}^{n+1/2}\mathbf{b}^{n+\alpha} + \mathbf{v}_{\perp j}^{n+\alpha}], \tag{7}$$

$$(dv_{\|j}/dt)^{n+1/2} = (-e/m_e)E_{\|}^{n+\alpha} - (\mu_j/m_e)\nabla_{\|}B^{n+\alpha}. \tag{8}$$

In the equations, $\mathbf{x}_j$ and $\mathbf{v}_j$ are the position and 3-D velocity of each particle, respectively, $v_{\|j}$, $\mathbf{v}_{\perp j}$ the parallel and perpendicular (guiding-center) velocities of the j-th particle, where $\mathbf{v}_{\perp j}$ includes the $E\times B$ and magnetic drifts. The diamagnetic current is separately calculated and added to $\mathbf{J}$ in Eq.(1) when the drift-kinetic equations are used. The quantity $\mathbf{b}$ is the unit vector along the magnetic field, e_j, m_j and μ_j the electric charge, mass and magnetic moment, respectively. It is remarked that the correction by the Poisson equation Eq.(3) ensures proper charge neutrality in the two-component plasma[13], since the required choice of $\alpha > \frac{1}{2}$ in Eq.(1) causes deviations from the charge continuity. (If this precaution is not observed, one will suffer from unrealistic charge separation[14].) Also we note that, unlike the hybrid-particle code, the electron inertia term is properly retained in the parallel motion in Eq.(8).

The accuracy of the macro-particle code has been tested in various circumstances. The MHD eigenmodes such as the Alfven and magnetosonic waves are correctly obtained in thermal equilibrium plasma[15]. In unstable plasmas, the frequency and growth rate agree

quite well with the theoretical ones for both the beam-driven and temperature anisotropy-driven Alfven ion-cyclotron (AIC) instability[13] and the kinetic Alfven wave[15,16] which is the Alfven wave with ion finite Larmor radius effects. For the AIC instability, a pitch-angle scattering process by the quasilinear effect is shown to be properly reproduced.

To start the simulations, a charge-neutral plasma of homogeneous density is initialized with the same number of ions and electrons (64 ions/cell) in the doubly-periodic Cartesian system (x, z). Three components of the particle velocity are generated according to a Boltzmann distribution of given temperatures. The ions located in the core of the flux loops are given an initial drift toward the positive y-direction to produce a pair of flux loops. The system size is $L_x = 400c/\omega_{pe}$ and $L_z = 300c/\omega_{pe}$ (note $c/\omega_{pe} = 7 \sim 15\lambda_{De}$). We use spatial grids with uneven spacings in the x direction, with $\Delta x \cong 0.55c/\omega_{pe}$ in the central region and $\Delta x \cong 1.6c/\omega_{pe}$ in the outer region; $\Delta z \cong 4.1c/\omega_{pe}$ in the z-direction. It is remarked that particle simulations have a reasonable resolution even with fewer grid points because the current and charge densities are less subject to spatial diffusion by virtue of solid Lagrangian particles[17].

The physical parameters are: the mass ratio $m_i/m_e = 25 - 200$, the temperature ratio $T_i/T_e = 1/8 - 49$, and the strength of the ambient toroidal (y-direction) magnetic field $\omega_{ce}^{(0)}/\omega_{pe} = 0 - 2$. The electron beta value is $\beta_e = 8\pi n T_e/B_0^2 = 0.04$, except for the runs with different values of electron thermal speed or the applied toroidal magnetic field. The time step is $\Delta t/\tau_A \cong 10^{-2}$, with $\tau_A \sim 4 \times 10^3 \omega_{pe}^{-1}$ the poloidal Alfven time, where $\tau_A = d/v_A$ with $v_A = B_p^{(0)}/\sqrt{4\pi n m_i}$ and d being half the initial separation of the flux loops. The parameters for the standard run described below in detail are: $m_i/m_e = 100$, $T_i/T_e = 1$ and $\omega_{ce}^{(0)}/\omega_{pe} = 1$. (Toroidal and poloidal stand for the y- and (x, z) components, respectively.)

3. Qualitative Results

3.1 Asymmetry due to parallel motion of electrons

Figure 1 is the time sequential plot of the poloidal flux function Ψ which is related to the poloidal magnetic field by $\mathbf{B}_p = \nabla \times (\Psi \hat{y})$. An elongated current layer with large negative current density ($J_y < 0$, opposite to those of the flux loops) is formed between the flux loops.

Magnetic reconnection proceeds most rapidly at the time $t \cong 1.9\tau_A$ shown in Fig.1(b). At later times the reconnection process is slowed down due to the repulsive force of the already reconnected field.

The enlargements of the plasma quantities in the rectangular region denoted in Fig.1(b) are shown in Figs.2 and 3. The first thing we notice is that the plasma ejection fans in the poloidal plane are thick and widely open in angle equally for electrons and ions. When we inspect Fig.2 more carefully, the poloidal current $J_p^{(s)}$, especially that of the electrons in Fig.2(a), shows a significant up/down asymmetry; the adjacent tips of the expansion fans are staggered, shifted either downward or upward in the left or right-half planes. An asymmetry is also seen in the ion poloidal current of Fig.2(b). The thickness of the current layer deduced from Fig.3(c), which is larger than the electron skin depth, is basically the same as that the asymmetry provides.

Since the poloidal plasma current is mostly due to the $E \times B$ drift in the presence of the ambient magnetic field[8], we subtract that part from the electron and ion currents to obtain $\delta \mathbf{J}_p^{(s)} = \mathbf{J}_p^{(s)} - q_s n_s V_E$, where $V_E = c\mathbf{E} \times \mathbf{B}/B^2$ and q_s, n_s are the charge and number densities of either electrons or ions. It is quite interesting in the middle panel of the figure that there remains in $\delta \mathbf{J}_p^{(s)}$ of both the electron and ion species a poloidal component that is comparable to $\mathbf{J}_p^{(s)}$. The electron component $\delta \mathbf{J}_p^{(e)}$ is quite asymmetric which directs leftward (rightward) in the upper (lower) half-plane. It is stronger on the flanks than at the center of the current layer. (The diamagnetic current has been subtracted from the electron component displayed in Fig.2(a).) The residual component for the ions $\delta \mathbf{J}_p^{(i)}$ mostly consists of the diamagnetic current due to the quadrupole density inhomogeneity shown in the bottom panel of Fig.2.

The origin of the asymmetry in Fig.2, which was observed in the macro-particle simulation[8], is disclosed in the following manner. First, note that the magnetic field, which is a sum of the toroidal field ($B_t > 0$) and the poloidal field represented by the contours of the poloidal flux function in Fig.3(c), is directed up-rightward and down-leftward in the upper and lower sides of the neutral line, respectively. Thus, the parallel electric field $E_{\|} = (\mathbf{E} \cdot \mathbf{B})/B$ in Fig.3(a), which is mainly the projection of the toroidal electric field E_y onto the local magnetic field, can accelerate the electrons *poloidally* rightward and leftward in the upper and lower half-planes, respectively. Indeed, the $E_{\|} < 0$ region in Fig.3(a) (dashed contours)

agrees quite well with the region where the asymmetric current exists. The directions of the parallel electric field $E_{||}$ coincide with those of the asymmetric poloidal currents shown in Fig.2(a). Since it takes a finite time for the incoming electrons into the current layer to get accelerated, the quantity $\delta \mathbf{J}_p^{(e)}$ should be stronger on the flanks of the current layer rather than at the X-point, as has been observed in Fig.2.

Moreover, we note that the region of the parallel electric field $E_{||} < 0$ is limited in the current layer due to charge neutralization elsewhere by thermal motion of electrons along the magnetic field [Fig.3(a)]. Therefore, after the electrons get a net parallel acceleration in the current layer, they pile up at the layer boundary where the parallel electric field vanishes, $E_{||} \to 0$. This results in local accumulation or depletion of the electrons within the current layer, namely, substantial quadrupole density inhomogeneity. Its magnitude is as large as $\delta n_s/n_0 \sim 0.3$ both for the electrons and ions, as already seen in the bottom panels of Fig.2.

The observed asymmetry caused by the electron parallel flow under an influence of the toroidally induced electric field is also verified by the following arguments. First, the magnetic drifts of the electrons have little to do with the asymmetry, as they are small in magnitude. Even omission of these terms in the simulation gives essentially the same result, as depicted in Fig.4(b). Second, a reversal of the direction (sign) of the ambient toroidal magnetic field causes the sign change of the parallel electric field. If the parallel electric field is driving the asymmetry, the up /down asymmetry should be also reversed, which is in fact the case as demonstrated in Fig.4(a).

The following simulation experiment gives a further evidence that the parallel flow of the electrons is a key ingredient of magnetic reconnection in the coalescence process. In the following special run, the spatial displacement of the electron element due to the parallel motion $v_{||}\mathbf{B}/|B|$ is ignored in a tiny region centered at the X-point, while keeping their parallel current $J_{||}^{(e)}$ and the poloidal motion in an ordinary fashion. The time history of the isolated poloidal magnetic flux contained in the flux loops is shown in Fig.5 with the solid line for the standard run. By clear contrast, for the special run the poloidal flux does not merge as demonstrated by the dashed line. In the latter run, a sharply peaked current layer is followed by a concentrated current vortex – a plasmoid at the X-point (Fig.6). The plasmoid is a natural consequence of slow removal of the current since the electrons (current

carrier) stay around the X-point for a long time.

A plasmoid is also seen for the cool electron case to be described in Sec.3.2. The plasmoid carrying $J_y < 0$ blocks a newly incoming plasma of the flux loops with $J_y > 0$ by exerting a repulsive magnetic force. With these figures, we can conclude that the parallel motion of the electrons is the origin of fast magnetic reconnection.

A discrepancy in the structures of the current layer between the present particle simulation and the collisionless two-fluid studies consists in the assumption of the fluid studies that the fluid motion be incompressible (divergence-free) separately with each species. This conclusion is obtained by comparing the particle simulation and the two-fluid study of the coalescence process[6]. (An active simulation experiment further verifying this point is to be described in Sec.3.3.) The latter study assumed $\nabla \cdot \mathbf{v} = 0$ with each plasma species. However, as will be stated in the next paragraph, the right condition is $\nabla \cdot (\mathbf{v}^{(e)} + \mathbf{v}^{(i)}) = 0$ across the electron and ion species. Although the divergence-free assumption with each plasma component allows us the use of the stream function for the flow, it rules out important non-symmetric solutions. Figure 4(c) shows the non-zero divergence of the electron current $\nabla \cdot \mathbf{J}^{(e)}$, which superimposes very well with the density perturbation in the bottom panel of Fig.2. Therefore, the flow compressibility cannot be ignored within the reconnection layer even in the presence of the ambient magnetic field.

The divergence of the current density $J_p^{(s)}$ in Fig.4(c) is found to be significant in the current layer, $|\nabla \cdot \mathbf{J}^{(s)}|/|\mathbf{J}^{(s)}| \sim 0.05(\omega_{pe}/c)$, or $D|\nabla \cdot \mathbf{J}^{(s)}|/|\mathbf{J}^{(s)}| \sim 0.2$, where D is the layer width. The divergence of the electron current arises from the parallel component, $\nabla \cdot \mathbf{J}^{(e)} \cong \nabla_{\|} \cdot \mathbf{J}_{\|}^{(e)}$. This is compensated by the divergence of the ion perpendicular current owing to the polarization drift ($v_{P\perp} \propto m_i$). The charge neutrality is maintained, $\nabla_{\|} \cdot \mathbf{J}_{\|}^{(e)} + \nabla_{\perp} \cdot \mathbf{J}_{\perp}^{(i)} \sim 0$. However, the divergence of each plasma flow leads to the aforementioned density inhomogeneity, as is typical for the low-frequency drift waves.

The diamagnetic current, $v_n = (v_{\perp}^2/2\omega_{ce})(\nabla n/n)$ with $\nabla n/n \sim 1/\ell_B$, due to the density hills and holes of the quadrupole shape generates the current perturbation and, hence, the toroidal magnetic field variation δB_t of the same form [Fig.3(d)]. Here, the gradient-B current is two orders of magnitude smaller than the diamagnetic current, since $\nabla B/B \sim (B_p/B_t)^2/2\ell_B$. Simultaneously, the change in the plasma density is associated with ap-

preciable change in the plasma pressure. The toroidal magnetic pressure and the plasma pressure is found to balance the poloidal magnetic pressure outside the current layer, as shown in Fig.4(d).

3.2 Electron thermal motion and plasmoid formation

In order to investigate the effect of the electron thermal motion, a run with half the electron thermal velocity compared to that of the standard run, i.e. $v_{te}/c = 0.1$, has been performed. A very interesting observation that is drastically different from the standard run (warm electrons) is the appearance of a "plasmoid" at the X-point, as shown in Fig.7. The poloidal magnetic field in the figure reveals that this plasmoid has a large "negative" (reconnection-blocking) toroidal current, which exerts a repulsive force on the incoming flux loops carrying the "positive" current and impedes the reconnection process.

It is emphasized here again that the divergence of the plasma flow, $\nabla \cdot \mathbf{V} \neq 0$, is essential for the full development of the plasmoid. For this reason, it is not surprising that one did not find this kind of the plasmoids in the incompressible fluid study of collisionless magnetic reconnection. By contrast, in the present study the plasma flow converging into the X-point is partly detached from the outgoing flow in the growth phase to merge and form a large vortex of the plasmoid. Indeed, the plasma flow in the poloidal plane shows a conformable flow encircling the plasmoid along the poloidal magnetic field of Fig.6. The size and magnitude of the encircling flow are intensified with the plasmoid growth.

As long as the plasmoid is trapped in the current layer, the plasma stays in a phase without magnetic reconnection. As the plasmoid grows, it is pushed sideways by the magnetic pressure and leaves the current layer at $t > 3\tau_A$. This happens because the configuration with the plasmoid at the center is unstable to a horizontal displacement. Note that the equations here allow for non-symmetric solutions. After the plasmoid is removed as shown in Fig.7(b), the process goes into the fast reconnection phase. The overall reconnection rate becomes about thirty percent smaller than that of the standard run with $v_{te}/c = 0.2$. However, for the real plasmas the removal time of the plasmoid will highly depend on the lateral length of the current layer.

The criterion to avoid the plasmoid formation is obtained in the following manner. The

average momentum equation for the electrons residing around the X-point may be approximated by, $nm_e dV_y/dt \sim -neE_y + nm_e \bar{V}_y/\tau_{th}$, where τ_{th} is the momentum loss time due to electron thermal motion. If the magnitude of the second term (loss) is larger than that of the first term (acceleration), the plasmoid can be avoided. As the average velocity of the X-point electrons is given by, $\bar{V}_y \sim (-eE_y/m_e)(\tau_r + \tau_{th})/2$, the above criterion is simply written as $\tau_{th} \leq \tau_r$, with τ_r the time for the electrons to come across the current layer of thickness D. Next, we note that the acceleration and loss times are approximately, $\tau_r \sim D/u_{in}$, and $\tau_{th} \sim L/(v_{th}B_p/B_t)$, respectively. Thus, the critical thermal speed of avoiding the plasmoid formation may be,

$$v_{th}^{crit} \geq u_{in} \frac{L}{D} \cdot \frac{B_t}{B_p} \,. \tag{9}$$

The parameters for the standard run, $u_{in} \sim 80(c/\omega_{pe})/5\tau_A$, $L/D \sim 30/5$, and $B_t/B_p \sim 1/0.2$, yield the critical thermal speed to be, $(v_{th}/c)^{crit} \sim 0.12$. This value is quite consistent with the simulation runs where the plasmoid is observed for the thermal speed of $v_{th}/c = 0.1$, whereas it is absent for the standard case with $v_{th}/c = 0.2$.

The laboratory and space plasmas that we are often interested in are considered to be in the warm electron regime. The ratio of the electron thermal speed and the (poloidal) Alfven speed which is a measure of electron bulk (fluid) motion is given by, $v_{te}/v_{Ap} \sim (\beta_e m_i/m_e)^{1/2}(B_t/B_p)$. If realistic parameters in these plasmas are used, i.e., $\beta_e \sim 0.05$ and $B_t/B_p \sim 5$, one has $v_{te}/v_{Ap} \sim 50$. On the other hand, the ratio for the standard run (warm plasma) of the particle simulation is $v_{te}/v_{Ap} \sim 20$. Thus, the electron thermal effects must be included in the study of collisionless magnetic reconnection unless the electron beta value is as low as $\beta_e \ll m_e/m_i$.

3.3 The incompressible fluid limit

As has been shown in Sec.3.1, the thickness of the current layer is larger than the electron skin depth, which arises from the internal structure. This implies that the reconnection rate, $d\Psi/dt \propto D/L$, should take a larger value than for the incompressible fluid limit where the layer thickness is much less than its width[6], $D/L \ll 1$. Although the particle simulation does not allow us to assume the $\nabla \cdot \mathbf{V} = 0$ condition, we can roughly emulate such limit

by increasing the magnitude of the toroidal magnetic field. This makes sense since the origin of the asymmetry – the poloidal projection of the parallel motion of the electrons, $v_{\|}^{eff} = (B_p/B_t)v_{\|}$, becomes small by increasing the toroidal to poloidal magnetic field ratio. Here, $v_{\|}$ stands for both the bulk and thermal velocities.

Fig.8 gives a comparison of the reconnection rates between the standard run and the run with a stronger toroidal magnetic field $\omega_{ce}/\omega_{pe} = 2$ (or $B_t/B_p \sim 10$). As is expected from the foregoing arguments on the role of the electron parallel motion, the reconnection rate for the stronger toroidal field in Fig.8 (dashed line) is reduced to two thirds that of the standard run, $d\Psi/dt \sim 0.13\Psi^{(0)}/\tau_A$.

The poloidal and toroidal electron current, the poloidal flux function and electron density are shown in Fig.9 for the run with $\omega_{ce}/\omega_{pe} = 2$. Even in this case, the anisotropy is seen in the plasma density as shown in Fig.9(d). It is noted that the slow reconnection here is not associated with a plasmoid mentioned in Sec.3.2 as the electron temperature is high ($v_{te}/c = 0.2$), but with an elongated current layer compared to that of the standard run in Fig.3(c). Also, the thickness of the current layer deduced from the poloidal flux function in Fig.9(c) is apparently narrower than for the standard case. The smaller value of D/L for larger B_t/B_p is just consistent with the smaller reconnection rate as shown in Fig.8. The present result might well show the flavor of the incompressible fluid limit without electron bulk and thermal effects for the given physical parameters.

4. Parametric Dependences

4.1 Ion inertia and Larmor radius effects

After we have confirmed the new features of fast collisionless magnetic reconnection, we proceed to investigate the reconnection speed of the flux loops. The reconnection rate is defined by the amount of decrease in the poloidal flux contained in either of the flux loops $\Delta\Psi$ during the time interval $\Delta\tau$ from the onset; the interval includes the most rapid phase of reconnection and is typically $\Delta\tau = 1.5\tau_A$. This definition is more reliable than reading off the maximum of time variations or the peak electric field intensity, since it can average out instantaneous fluctuations arising from time-and-space non-smoothness in particle simulations.

Figure 10(a) shows a dependence of the reconnection rate on the ion inertia. In this series of the runs the mass ratio (m_i/m_e) is varied keeping the electron mass fixed. The reconnection rate becomes a smoothly increasing function of ion mass without a sudden curvature change in the wide range. The typical reconnection time of $[(1/\Psi)d\Psi/dt]^{-1} \sim 5\tau_A$ in Fig.10 is shorter than that obtained by the two-fluid simulation without thermal effects (Sec.3.3); in the latter a sharp rise occurs in the reconnection rate at the small ion mass[6]. The present observation that the current layer thickness changes only smoothly with the increase in the ion mass because of the internal structure is in line with the smooth increase in the reconnection rate.

A dependence on the ion Larmor radius is rather insensitive when the radius is small compared to the ion skin depth, $\rho_i < c/\omega_{pi} \propto (m_i/m_e)^{1/2}$ ($c/\omega_{pi} = 5c/\omega_{pe}$ for $m_i/m_e = 25$). When the above criterion is not met by increasing the ion temperature for the fixed toroidal magnetic field, a drastic reduction of the reconnection rate takes places as observed in Fig.10(b). The dependence on the ion Larmor radius for the $m_i/m_e = 100$ case in the panel (b) ($c/\omega_{pi} = 10c/\omega_{pe}$) and that for the two lines of $\rho_i = 1 - 2c/\omega_{pe}$ in the panel (a) are well fitted with the decreasing function F of the ion Larmor radius divided by the ion skin depth,

$$d\Psi/d\tau \;=\; F(\rho_i/(c/\omega_{pi}) \times (m_i/m_e)^{(1-\nu)/2}). \qquad (10)$$

Here, the value of the exponent is $\nu \cong 2.7$ and the $F(x)$ profile is given by Fig.10(b). The mass dependence in Eq.(10) is $F((m_i/m_e)^{(1-\nu)/2})$. Thus, we expect the ion Larmor radius effect to occur at $\rho_i/(c/\omega_{pi}) \sim 10$ for $m_i/m_e = 1836$. For large ion Larmor radius case, the ions are unmagnetized and detached from the electron element; the ions do not follow the $E \times B$ drift motion with which the electron poloidal motion is well described. An electrostatic effect may take a role in this case. Thus, one needs to formulate non-perturbative theory to analyze this nonlinear kinetic regime.

4.2 Compressible effects under weak magnetic field

A dependence on the strength of the applied toroidal magnetic field is another issue of interest. Both the electron and ion dynamics is affected in this case, unlike the case described above in Sec.4.1. The simulation results using the full-kinetic version of the macro-particle

code are plotted for the magnetic field ratio of $B_t/B_p \cong 0$ and 1 vertically along the constant ion mass, $m_i/m_e = 100$ in Fig.10(a). For intermediate value of the toroidal magnetic field, $B_t/B_p \sim 1$, the plasma flow is still asymmetric. But, the plasma density in the current layer increases as a whole by compressional effect, unlike the localized compression of quadrupole shape in the large toroidal field case $B_t/B_p \gg 1$ in Sec.3. An elongated high-density channel is formed, $<n_s>/n_0 \sim 1.5$. The ejected flow forms a widely open expansion fan which is characteristic of the X-type reconnection. The reconnection rate (denoted by the open square) increases about 20 percent compared with the standard run.

On the other hand, when the ambient toroidal magnetic field is absent, the plasma flow becomes symmetric (see Fig.6 of Ref.9). The magnetic neutral layer is highly compressed in density, $<n_s>/n_0 \sim 2.1$. The reconnection rate further increases as shown by the filled square in Fig.10(a). The experimental formula for the density of the current layer is given by,

$$< n_s > \sim n_0(2+\epsilon)/(1+\epsilon), \tag{11}$$

with the magnetic field ratio $\epsilon = B_t/B_p$. From a simplified model balancing the incoming and outgoing mass fluxes in the square box reconnection layer, the reconnection rate may be scaled as,

$$d\Psi/d\tau \propto v_A D/L \sim v_A < n_s > /n_0 \propto \sqrt{< n_s >}. \tag{12}$$

The reconnection rate estimated using Eqs.(11) and (12) roughly agrees with that due to plasma compressibility observed in Fig.10(a).

Finally, a run with half the system size is described to examine further the role of the electron inertia (the electron thermal speed is also halved to keep the beta value constant for the fixed amount of current in the flux loops). The reconnection rate does increase as shown by the (+) symbol in Fig.10(a). This is a significant level of increase since the lower electron temperature tends to suppress the reconnection rate as described in Sec.3.2. It is concluded, therefore, that the collisionless reconnection rate of the coalescence process is a function of both the ion and electron masses. This again confirms that both the bulk and thermal motions of the electrons along the magnetic field play roles in collisionless magnetic

reconnection.

5. Summary and Conclusion

In this paper, it has been shown for the first time that both the bulk and thermal motions of the electrons along the magnetic field play significant roles in collisionless reconnection of the magnetic flux loops. Namely, the asymmetric plasma flow and density variation are direct consequences of divergence of the bulk electron motion along the ambient magnetic field. The plasma flow has been shown to be locally divergent, $\nabla \cdot \mathbf{V}^{(s)} \neq 0$ $(s = i, e)$, within the current layer even in the presence of the toroidal magnetic field. The asymmetry and internal structure lead to a thick current layer whose thickness is larger than the electron skin depth. The plasma ejection fans in the poloidal plane are widely and equally open in angle both for the ions and electrons, which rapidly remove the reconnection-blocking toroidal current out of the X-point region. These new features enhance the reconnection rate compared with the incompressible fluid case where the layer thickness becomes singularly thin.

Moreover, it has been shown that the asymmetric plasma flow and the quadrupole density inhomogeneity constitute a natural solution of the collisionless coalescence process. The asymmetric solution is obtained if one removes the incompressible assumption traditionally imposed on each plasma species in the fluid studies. This point has been verified by an additional run with a larger B_t/B_p ratio by which the origin of the asymmetry – (the poloidal projection of) the electron parallel motion is suppressed. This case of emulating the fluid limit results in the narrower and more elongated current layer, and slower reconnection. Because of these new features, the parametric dependence of the reconnection rate becomes a smoothly increasing function of the ion mass including the small mass regime.

When the electron mass diffusivity along the magnetic field is small due to low parallel temperature $\beta_e \ll m_e/m_i$, a plasmoid is created in the current layer. In this case, the pump-out rate of the current accumulated at the X-point is not large enough to avoid the formation of the plasmoid because of the long residence time of the current-carrier electrons around the X-point region. The plasmoid efficiently impedes magnetic reconnection by acting a repulsive force on the incoming flux loops. The divergence of the plasma flow, $\nabla \cdot \mathbf{V}^{(s)} \neq 0$,

is again essential in the development of the large *detached* plasmoid. On the other hand, the criterion of avoiding the plasmoid formation, Eq.(9), has been obtained in terms of the critical thermal speed.

The plasmoid has also been observed if the spatial movement of the electrons along the magnetic field is artificially discarded at the X-point while including its parallel current in an ordinary fashion. Thus, the plasmoid appears whenever the parallel electron flow is stagnant or suppressed at the X-point. These are the strong evidences to reveal that the parallel motion of the electrons along the magnetic field, both bulk and thermal, is a key physics component in collisionless reconnection of the magnetic flux loops.

The effect of the finite ion Larmor radius has been found to reduce the reconnection rate drastically when it exceeds the ion skin depth. The empirical scaling of the reconnection rate Eq.(10) has been obtained. This nonlinear regime needs a comprehensive kinetic study including both electrostatic and magnetic effects. On the other hand, the plasma compressibility under the weak toroidal magnetic field has been shown to increase the reconnection rate, as given by Eqs.(11) and (12). This is a similar phenomenon as in the resistive fluid case[18].

Acknowledgments

The author acknowledges useful discussions with Dr.D.Biskamp, where prominent disparities between the particle and incompressible fluid simulations let the author to motivate the present study. He wishes to thank Professor B.Coppi and Dr.S.Miglioulo for profitable discussions when he was engaged in the study of the electron thermal effect, and Professor A.Nishida, Dr.S.Machida and Dr.K.Shibata for general discussions and encouragements.

References

1. H.P.Furth, P.H.Rutherfort, and H.Selberg, Phys.Fluids, 16, 1054 (1973).
2. B.B.Kadomtsev, Fiz.Plasmy, 1, 710 (1975) [Sov.J.Plasma Phys., 1, 389 (1975)].
3. A.Y.Aydemir, Phys.Fluids, B2, 2135 (1990).
4. M.Ottaviani and F.Porcelli, Phys.Rev.Lett., 71, 3802 (1993).
5. B.Rogers and L.Zhakarov, Phys.Plasmas, 2, 3420 (1995).
6. D.Biskamp, E.Schwarz, and J.F.Drake, Phys.Rev.Lett., 75, 3850 (1995).
7. T.Tajima, F.Brunel and J.Sakai, Astrophys.J., 258, L45 (1982).
8. M.Tanaka, Phys.Plasmas, 2, 2920 (1995).
9. M.Tanaka, Comput.Phys.Commun., 87, 117 (1995).
10. M.Tanaka, Bull.Amer.Phys.Soc., 40, 1877 (1995).
11. J.A.Wesson, Nucl.Fusion, 30, 2545 (1990).
12. E.R.Priest, Solar Magnetohydrodynamics, (D.Reidel, Holland, 1982).
13. M.Tanaka, J.Comput.Phys., 107, 124 (1993).
14. R.Horiuchi and T.Sato, Phys.Plasmas, 39, 3587 (1994).
15. M.Tanaka, J.Comput.Phys., 79, 209 (1988).
16. A.Hasegawa and L.Chen, Phys.Fluids, 19, 1924 (1976).
17. D.Sulsky, S-J.Zhou, and H.L.Schreyer, Comput.Phys.Commun., 87, 236 (1995).
18. A.Bhattachargee, F.Brunel, and T.Tajima, Phys.Fluids, 26, 3332 (1983).

Figure Captions

Fig.1. Time development of the poloidal flux function for the standard run in (a) the equilibrium state at $t = 0.75\tau_A$, (b) the most rapid phase of reconnection at $t \cong 1.9\tau_A$, and (c) at $t = 2.5\tau_A$.

Fig.2. The enlargements of the poloidal current $J_p^{(s)}$, the residual current with the $E \times B$ component subtracted $\delta J_p^{(s)}$, and the number density n_s in the square region denoted in Fig.1(b), from top to bottom, respectively. The column (a) is for the electrons and (b) for the ions. (Diamagnetic current has been subtracted in (a), and $\delta n_s/n_0 \sim 0.3$.) Dashed contour lines correspond to negative values of the function.

Fig.3. The enlargements of (a) the parallel electric field $E_{\|}$, (b) the electrostatic potential φ, (c) the poloidal flux function Ψ, and (d) the perturbed toroidal magnetic field δB_t at $t \cong 1.9\tau_A$ of the standard run. The maximum strengths are $E_{\|} \sim 7.4 \times 10^{-4}$, $\varphi \sim 0.16$, $\Psi \sim 8.7$, and $\delta B_t \sim 2.4 \times 10^{-2}$.

Fig.4. The enlargements of the electron poloidal current for (a) the $B_t < 0$ run, and (b) the run ignoring the electron magnetic drifts. (c) The divergence of the electron current, and (d) the cross-cut of the plasma and magnetic pressures vertically through the current layer at $z = 0.41L_z$ for the standard run.

Fig.5. The time history of the isolated poloidal flux for the standard run (solid) and for the special run (dashed) in which the spatial displacement of the electrons at the X-point is discarded while keeping the toroidal current.

Fig.6. The poloidal and toroidal magnetic field for $t = 3\tau_A$ of the run shown with the dashed line in Fig.5. The plasmoid stays at the X-point and impedes magnetic reconnection.

Fig.7. The enlargements of the poloidal (upper) and toroidal (lower) magnetic field at (a) $t = 2.5\tau_A$ and (b) $t = 3.0\tau_A$ for the cool electron case. The appearance and lateral movement of the plasmoid are observed in the current layer.

Fig.8. The time history of the isolated poloidal flux for the standard run (solid) and for the run with the stronger toroidal magnetic field, $B_t/B_p \sim 10$ (dashed).

Fig.9. The enlargements of (a)(b) the electron poloidal and toroidal current, respectively, (c) the poloidal flux function, and (d) the electron number density at $t = 1.9\tau_A$ of the run with the stronger toroidal magnetic field, $B_t/B_p \sim 10$.

Fig.10. The parametric dependences of the reconnection rate on (a) the ion mass ($\rho_i = 1$, $2c/\omega_{pe}$), and (b) the ion Larmor radius ($m_i/m_e = 100$, fixed). Also in (a), the reconnection rates for the applied toroidal magnetic field of $B_t = 0$, 0.2 and for half the system size are plotted with squares and the (+) symbol, respectively.

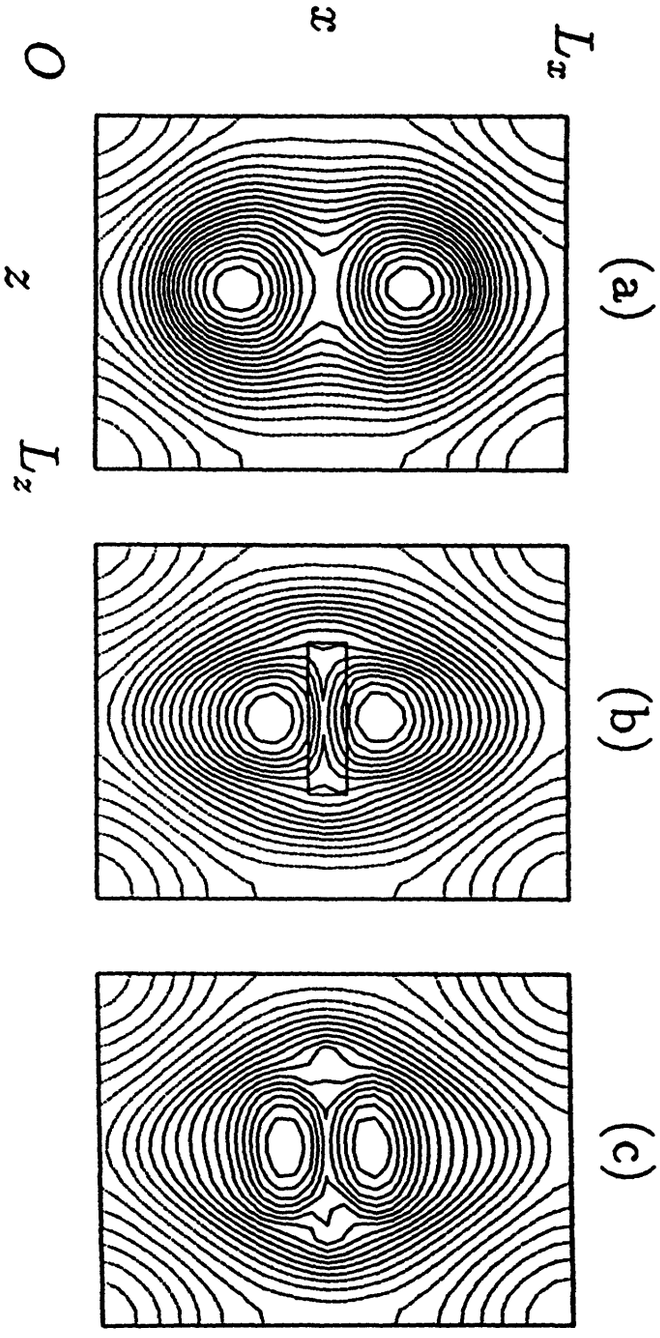

Figure 1.

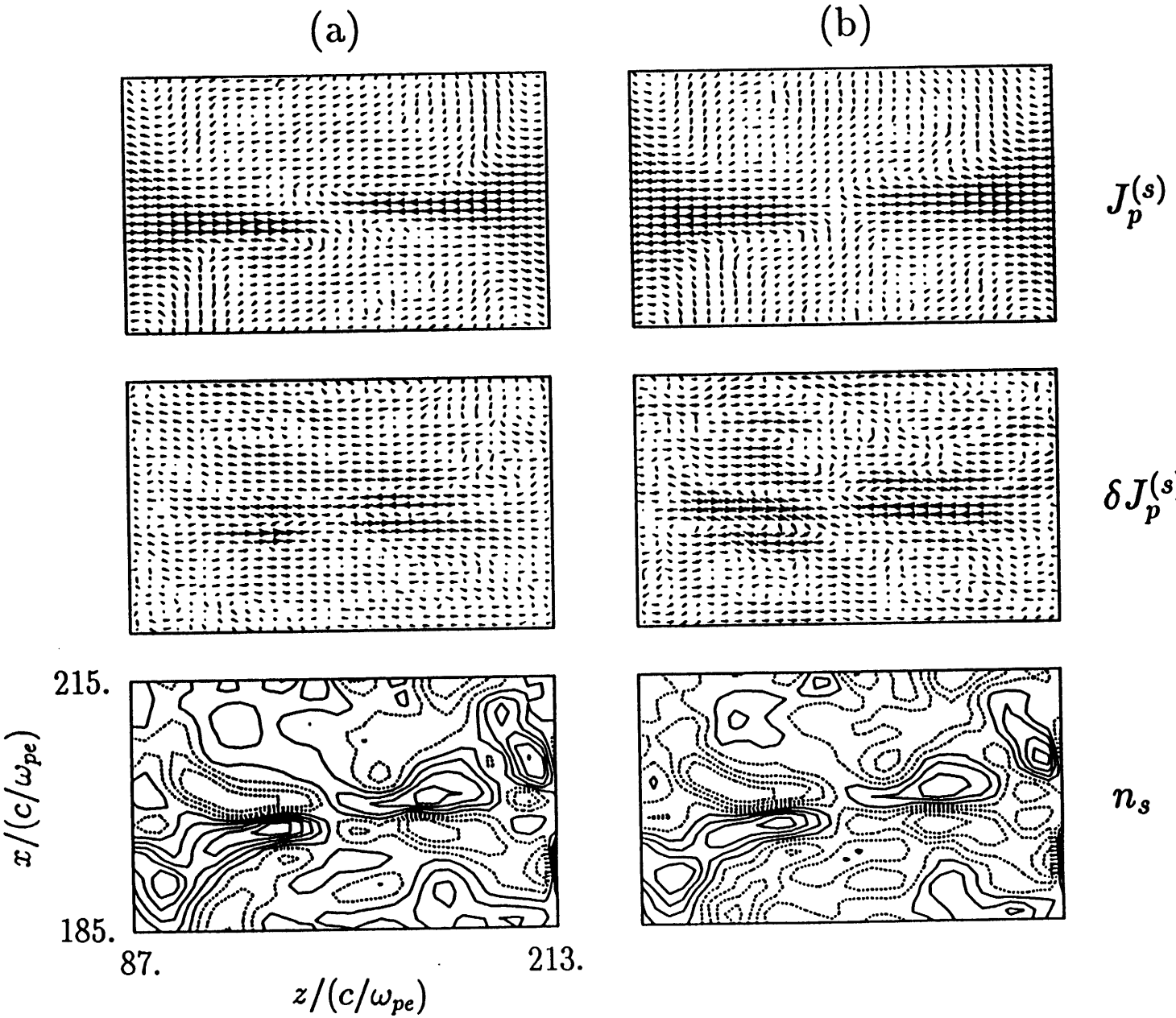

Figure 2.

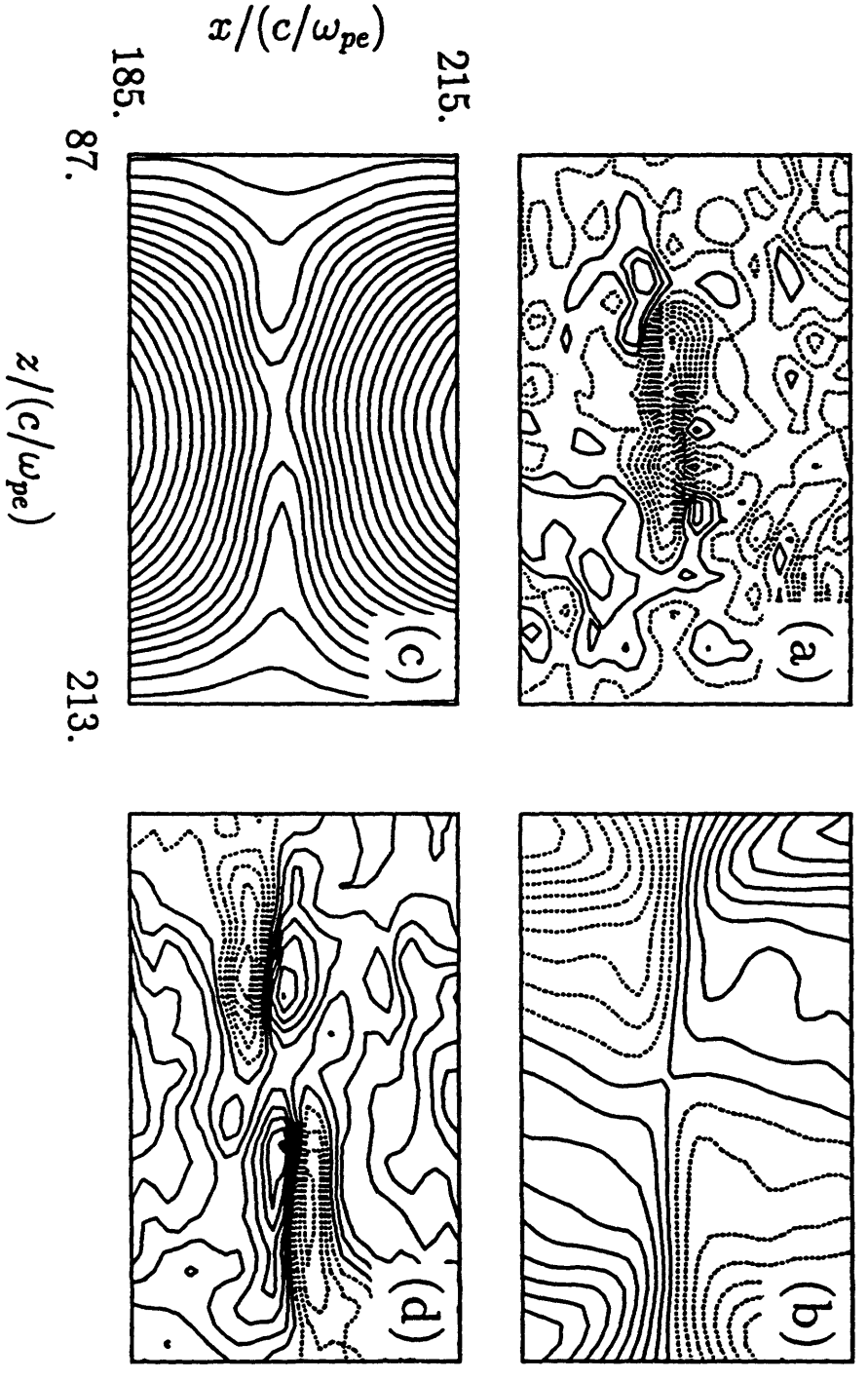

Figure 3.

Figure 4.

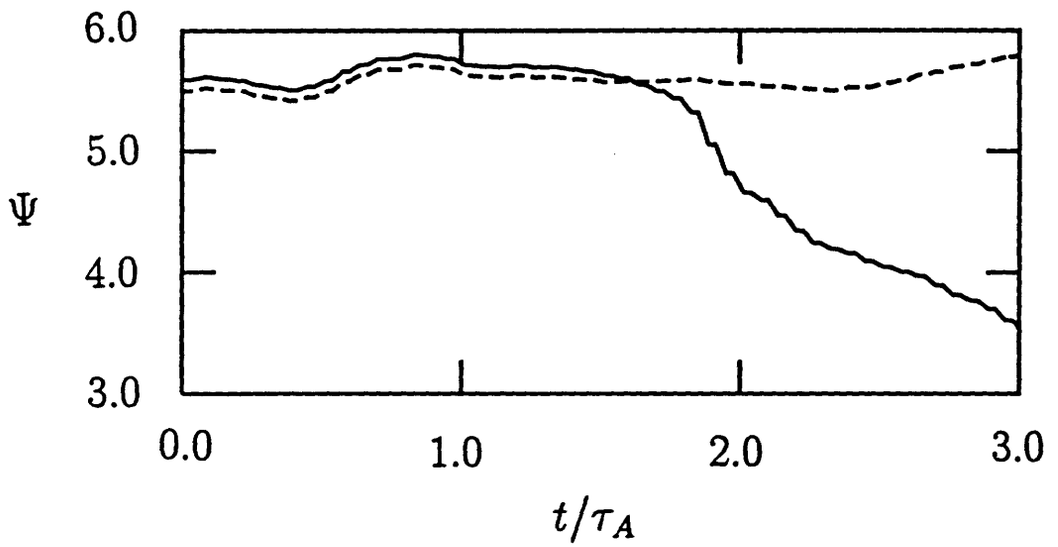

Figure 5.

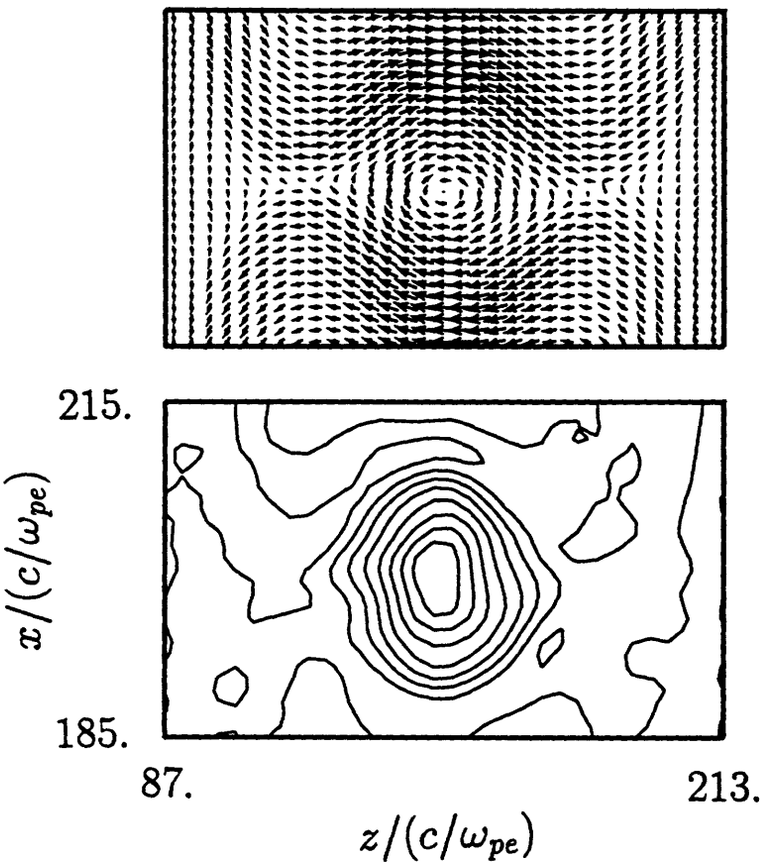

Figure 6.

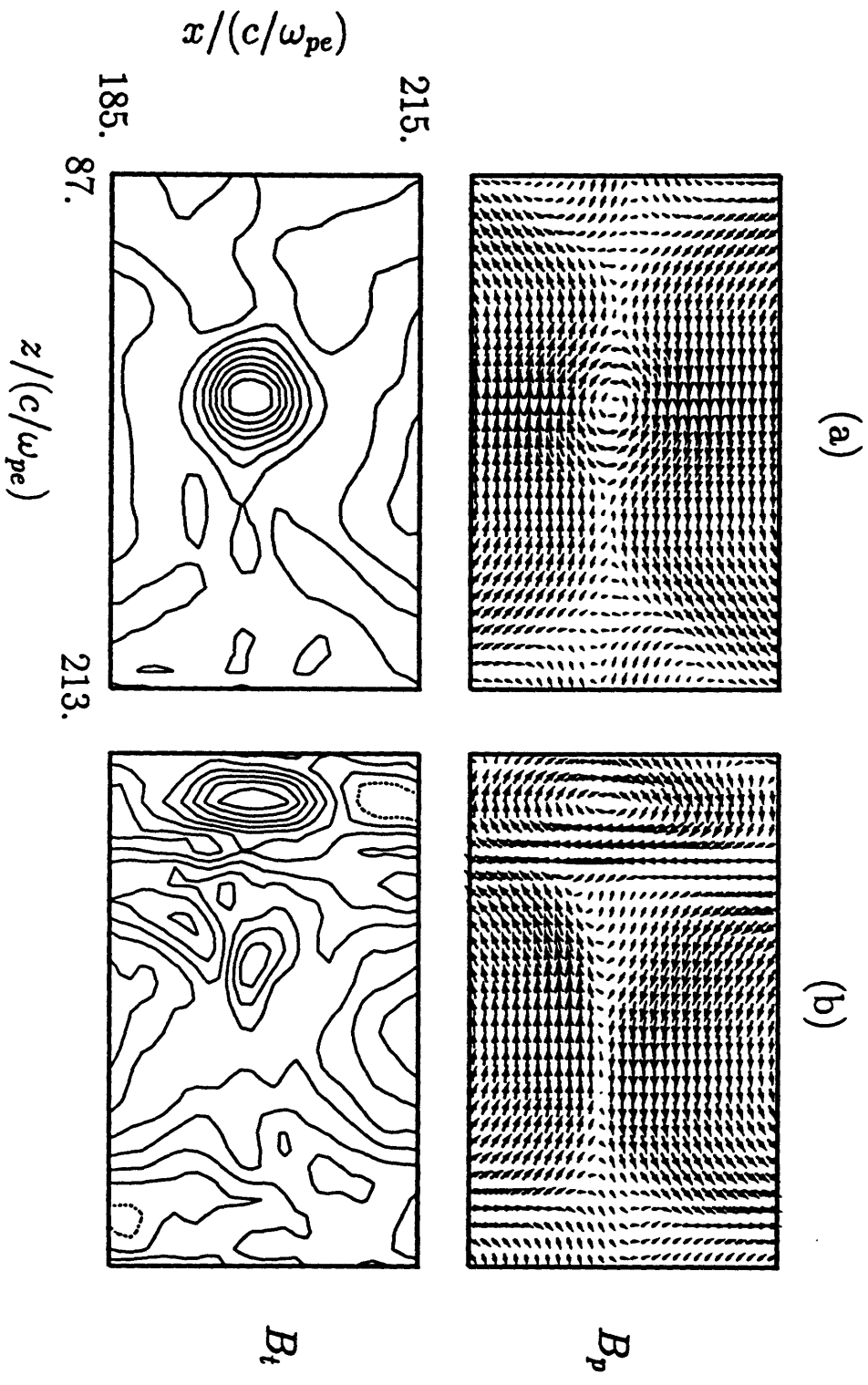

Figure 7.

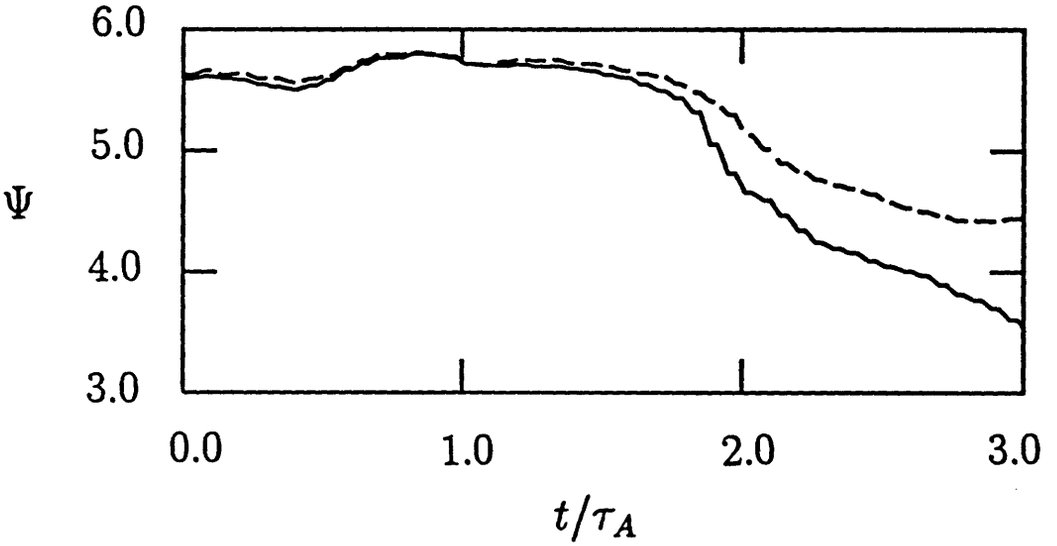

Figure 8.

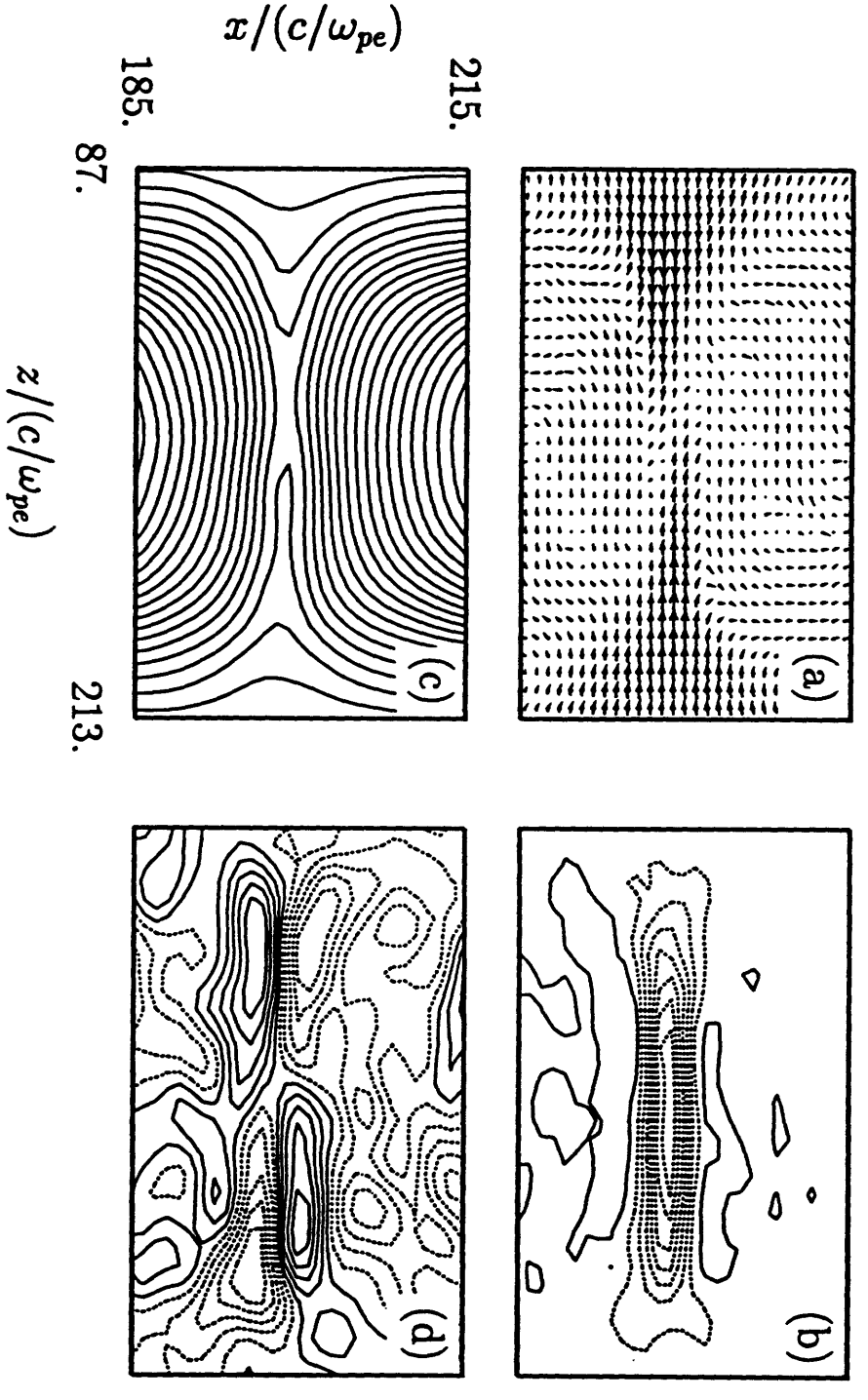

Figure 9.

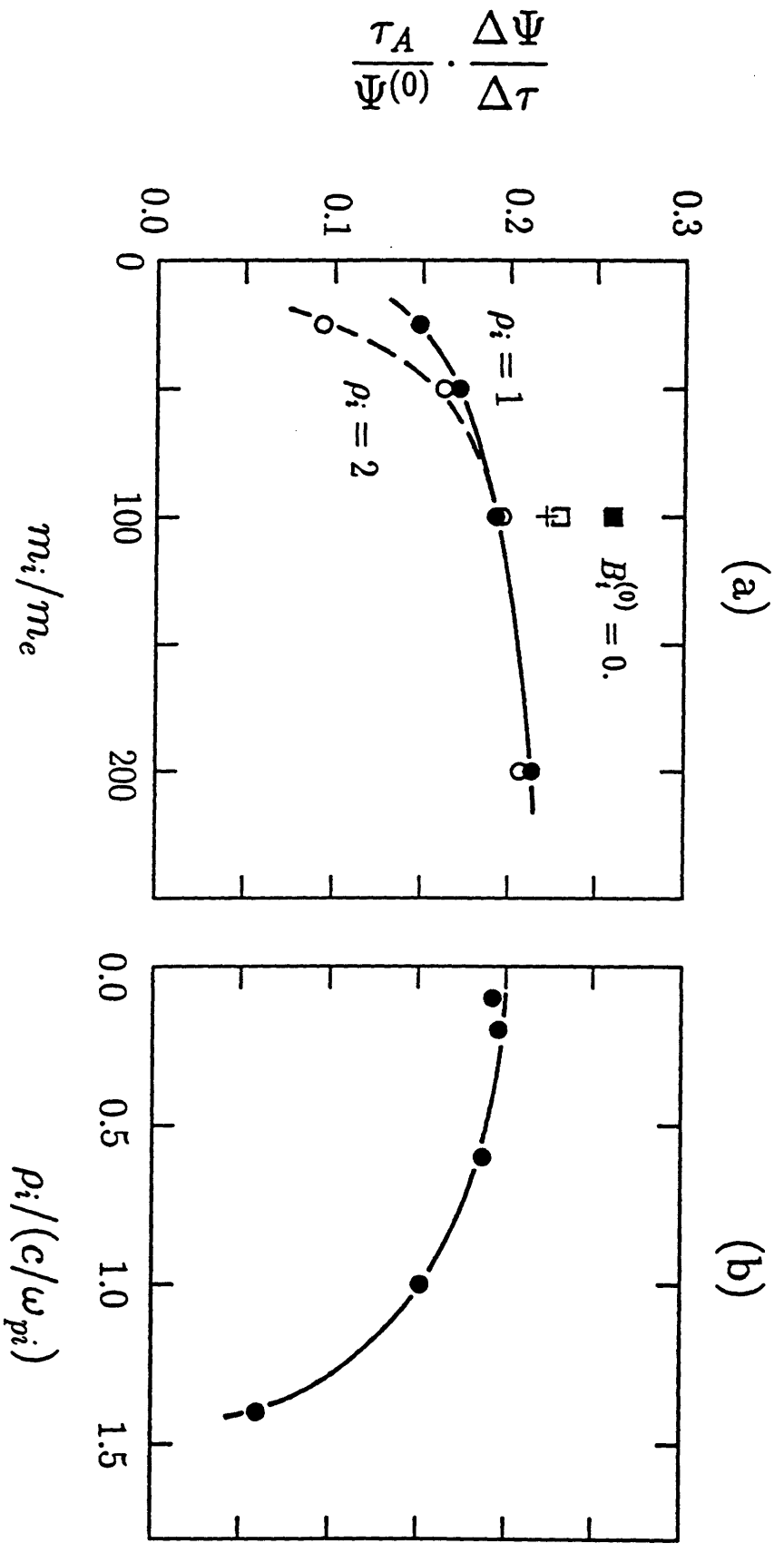
$\frac{\tau_A}{\Psi(0)} \cdot \frac{\Delta\Psi}{\Delta\tau}$
0.0
0.1
0.2
0.3
0
100
200
m_i/m_e
$\rho_i = 1$
$\rho_i = 2$
$B_t^{(0)} = 0.$
(a)
0.0
0.5
1.0
1.5
$\rho_i/(c/\omega_{pi})$
(b)

Figure 10.